RSC Advances

ROYAL SOCIETY OF CHEMISTRY

www.rsc.org/advances

Journal Name RSCPublishing

ARTICLE

Synthesis and Characterization of Ni Doped SnO_2 Microspheres with Enhanced Visible-light Photocatalytic Activity

Cite this: DOI: 10.1039/x0xx00000x

Received 00th January 2012,
Accepted 00th January 2012

DOI: 10.1039/x0xx00000x

www.rsc.org/

Huan Chen, Liyong Ding, Wen Sun, Qingqing Jiang, Juncheng Hu*, Jinlin Li

Nickel-doped tin dioxide (NDT) microspheres with various doping levels were prepared by hydrothermal synthesis and characterized by using X-ray powder diffraction, scanning electron microscopy, transmission electron microscopy, high-resolution transmission electron microscopy, energy-dispersive spectroscopy analysis, Fourier Transform infrared spectroscopy, X-ray photoelectron spectroscopy, and UV−vis absorption spectroscopy. The formation mechanism of NDT microspheres was discussed. All samples prepared with different Sn/Ni ratios shows higher photocatalytic activity than that of pure SnO_2 and pure NiO under visible light irradiation ($\lambda > 420$ nm). The photocatalytic activity closely relate to the composition of as-prepared photocatalysts. It is noted that the NDT microspheres with the doping content of 33.3 mol% exhibits the highest photoactivity. Moreover, this catalyst showed improved stability, and the activity did not weaken significantly after four recycles. The higher activity of NDT microspheres may be attributed to the combined effect of its demonstrated doping levels, appropriate band gap. And the doping of Ni^{2+} may facilitate the generation of electrons and holes pairs and inhibit their recombination rate by act as a temporary trapping sites of photoinduced electrons.

Introduction

Environmental problems are harmful to human health. The organic pollutants and toxic water pollutants are difficult to degrade by natural means. Semiconductor photocatalysts have been widely used to solve many environment-related issues recently because of low toxicity, low cost, recyclability, and the ability to facilitate multielectron transfer processes.[1] Traditional semiconductor materials, such as TiO_2,[2] Fe_2O_3 and CdS,[3] suffer from low responsive to visible light, high electron-hole recombination or photocorrosion. Hence, researches in this field therefore pay more attention on novel ones which are equipped with highly photocatalytic activity. Because of sunlight's distinct advantages of being clean, accessible and inexhaustible[4] for environmental mediation.[5] However, visible light accounts for about 50% of the sunlight. To make full use of visible light, it is satisfying to exploit novel visible light sensitive semiconductor photocatalysts.[6] Because of SnO_2 with low cost, photochemical stability, high activity for many photocatalytic reactions, it has raised very strong interest for various technologically important applications in lithium batteries,[7] gas sensing,[8,9] as well as in photcatalysis.[10,11] However, the instinct band-gap of SnO_2 (ca. 3.6 eV) limits the absorption ability of visible light of the sunlight, which results in the relatively low efficiency.

Modification is one of the effective approaches to promote the light absorption, which the preparation of visible light sensitive photocatalysts could be based on. Such as by doping transition metals (e.g., Cr, Ni and Mn) or nonmetals (e.g., C, N and S) into TiO_2 to extend its absorption edge to visible region.[12] In order to improve visible light absorption ability of SnO_2, efforts have been done in the controlled synthesis of semiconductor oxides with doped metals, such as Zn-doped SnO_2 and Sn-doped Fe_2O_3.[13,14] It has been disclosed that several dopants (Mn, Al, Cr, Co, Mg, Cu, Fe) can escort to enhance the properties of SnO_2,[15] which is able to improve the photoactivity of photocatalysts, this is the origin of our research impetus. Many papers have reported that nickel-doped tin dioxide nannomaterials have outstanding gas sensing properties than that of other materials.[16] However, only few of them focused on the photocatalytic properties of SnO_2.

Herein, we successfully synthesized a series of nickel-doped tin dioxide (NDT) microspheres for photo-degradation of rhodamine B solution. The catalytic efficiency for the degradation of the dyes was affected by different Ni dopant concentrations. At room temperature, the as-prepared NDT microspheres have higher photocatalytic activity compared to pure SnO_2 and pure NiO. The causes of the NDT microspheres for visible-light absorption were investigated and discussed in terms of the changes of energy band structure. The incorporation of Ni^{2+} into the SnO_2 lattice can also provide them with intriguing properties inherited from the synergetic effect and the radius of Ni^{2+} is smaller than that of Sn^{4+}. Furthermore, we reported a simple one-pot method to prepare these catalysts. Different from other method, this method has several advantages, including low-temperature preparation, accurate control of the stoichiometry. For the preparation of NDT microspheres, the hydrothermal method, where Ni^{2+} and Sn^{4+} were used as starting reagents, had been demonstrated to be an effective approach. After calcinations, we can obtain NDT microspheres with high crystallinity. The unique structures may show improved properties and promising applications in many fields.

Experimental

Synthesis of NDT Microspheres

In a typical synthesis of NDT microspheres, a solution having the molar ratio of Sn/Ni = 2:1 was prepared by dissolving stoichiometric amounts of $SnCl_4•5H_2O$ and $Ni(NO_3)_2•4H_2O$ in 70 mL of absolute methanol. After the $SnCl_4•5H_2O$ and $Ni(NO_3)_2•4H_2O$ totally dissolved, a certain amount of urea and benzyl alcohol was added to the mixture in the ratio urea: BZ = 0.5:2 (molar ratio). After stirring for 1 h, the solution was transferred to a teflon reactor (100 mL) and autoclaved at 180 °C for 5 h. The resulting product was isolated by centrifugation and washed three times with deionized water and dried at 60 °C for 24 h. The product was calcined in air at 350 °C for 5 h. The preparations of other NDT microspheres were carried out using the same procedure with different molar ratios of the metal precursors.

Characterization of the Catalyst

The crystalline structure of the photocatalysis were characterized by powder X–ray diffraction (XRD) employing a scanning rate of 0.05 °/s in a 2θ range from 10 to 80° , using a Bruker D8 advance instrument equipped with monochromatized Cu-Kα radiation. The morphologies and particle sizes of the samples were observed by an SU-8000 field-emission scanning electron microscope (FESEM, Hitachi, Japan) at an accelerating voltage of 3 kV. Energy dispersive spectrum analysis (EDS) system was connected to the SEM. Transmission electron microscopy (TEM) test was conducted by a Tecnai G20 (FEI Co, the Netherlands) using an accelerating voltage of 200 kV. X-ray photoelectron spectroscopy (XPS) was recorded on a VG Multilab 2000 (VG Inc.) photoelectron spectrometer using monochromatic Al Ka radiation undervacuum at 2×10^{-6} Pa. All the binding energies were referenced to the C_{1s} peak at 284.8 eV of the surface adventitious carbon. The real composition of composites were analyzed using a PerkinElmer NexION 300x Inductively coupled plasma mass spectrometer (ICP-MS). The UV-vis DRS were collected using a Shimadzu UV-2450 spectrophotometer from 200 to 800 nm using $BaSO_4$ as background. The Fourier Transform infrared spectroscopy (FTIR) were recorded on a Nicolet NEXUS 470 (Nicolet Instruments, Offenbach, Germany) FTIR ESR using KBr as background.

Catalyst Activity Test

The photoactivity of the samples was tested by the degradation of RhB under visible light irradiation. In a typical experiment, 50 mg of the photocatalyst and 50 mL of aqueous solution of RhB (1.0×10^{-5} mol/L; 50 mL) were added into a flask, then the mixed solution was oscillated in the dark overnight. After reaching adsorption equilibrium, the photocatalytic reaction was initiated by irradiating the system with a 350W xenon lamp ($\lambda > 420$ nm, use a cutoff filter of 420 nm). At given intervals, 4 mL aliquots were collected, centrifuged, and then filtered to remove the catalyst particles for analysis. The filtrates were finally analyzed using a UV-vis spectrophotometer (UV-2450).

The formation of •OH on the surface of the UV illuminated samples was detected by a photoluminescence (PL) method using coumarin as a probe molecule. Coumarincan readily react with •OH to produce the highly fluorescent product, 7-hydroxycoumarin (7HC) (umbelliferone). The experimental procedure was similar to the measurement of photocatalytic activity. In a typical process, 50 mg of the photocatalyst and coumarins (50 mL, 5.0×10^{-4} M) were mixed under magnetic stirringfor 4 h under dark conditions. After visible light irradiation for 10 min, the reactionsolution was filtered to measure the increase in the PL intensity around 445 nm excited by 332 nm light.

To detect the active species during the photocatalytic reaction, the presence of superoxide radicals ($\cdot O_2^-$), hydroxyl radicals (·OH) and holes (h^+) were investigated by adding benzoquinone (BQ), isopropanol (IPA) and triethanol amine(TEOA) as scavengers, respectively. The scavengers were introduced into the RhB solution prior to the addition of the photocatalysts using a similar procedure to that described in above.

Results and discussion

Fig. 1 shows the XRD patterns of as-synthesized samples. Pattern (a) can be indexed to orthorhombic structure SnO_2 (JCPDS 41-1445), characteristic peaks at 26.6˚, 33.9˚ and 51.8˚ can be assigned to the diffraction planes of (1 1 0), (1 0 1) and (2 1 1).[17] No other peaks are observed indicating that $Sn(OH)_4$ formed firstly, and the further dehydration of $Sn(OH)_4$ generated SnO_2 nanoparticles. When Ni are introduced to the synthesis, the formation of both SnO_2 and $Ni(OH)_2$ can be observed for the as-synthesized microspheres before calcination. After calcination at 350 °C for 5 h, with the introduction of higher amounts of Ni, the characteristic peaks become wider and shift toward lower 2θ values. These could be attributed to the decrease of grain size and the insertion of smaller radius atoms, like Ni^{2+} here. Moreover, the successive peak shift indicates that the as-prepared product is not a physical mixture, but the Ni species such are incorporated into the lattice of SnO_2 and form solid solutions probably. However, the only observed diffraction peaks belong to SnO_2, as showed in Fig. 1. This further confirm the formation of a single phase resulting in successful doping of Ni into SnO_2. The slight shift toward lower 2θ values are believed to be related to the decrease of the length of the SnO_2 crystal lattice, which is attributed to a lower ionic radius of Ni^{2+} (0.69 Å) campared with Sn^{4+} (0.83 Å). This further confirm that the Ni ions are incorporated into the SnO_2. This can be clearly observed from the Fig. 1 inset.

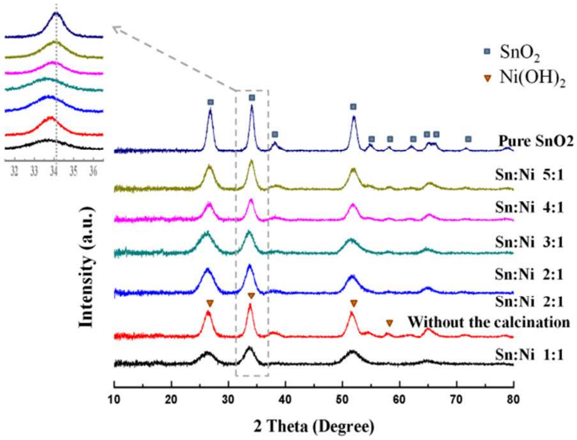

Fig. 1. XRD patterns of Ni-doped SnO_2 (NDT) microspheres with different ratios of Sn:Ni. The inset is the enlarged (101) peak of Ni-doped SnO_2.

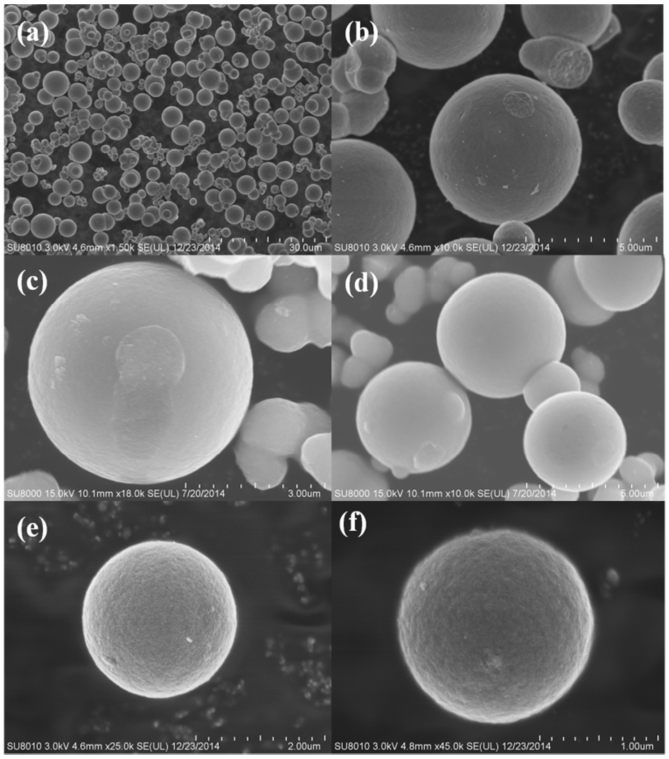

Fig. 2. SEM images of the as-prepared NDT microspheres. (a), (b) Sn/Ni of 5:1, (c) ,(d) Sn/Ni of 3:1, (e) Sn/Ni of 2:1 and (f) Sn/Ni of 1:1.

Then we studied the morphology of prepared samples. It can be seen from Fig. 2 that these NDT samples are presented to be microspheres, no other morphologies can be observed. However, the sizes of corresponding NDT microspheres are significantly different. With the increase of Ni doping level, the average diameter of NDT microspheres decreased gradually. For Sn/Ni of 5:1 and Sn/Ni of 3:1, it is clearly that numerous microspheres with an average diameter of about 5–6 μm and 3–4 μm respectively. Moreover, it is obvious that the surface of the sphere was smooth. For Sn/Ni of 2:1 (2μm) and Sn/Ni of 1:1 (1.5μm) , it clearly displays the surfaces of spheres are rough and the spheres are constructed from fine particles. And the aggregations are relatively uniform and tend to form regular spherical morphologies.

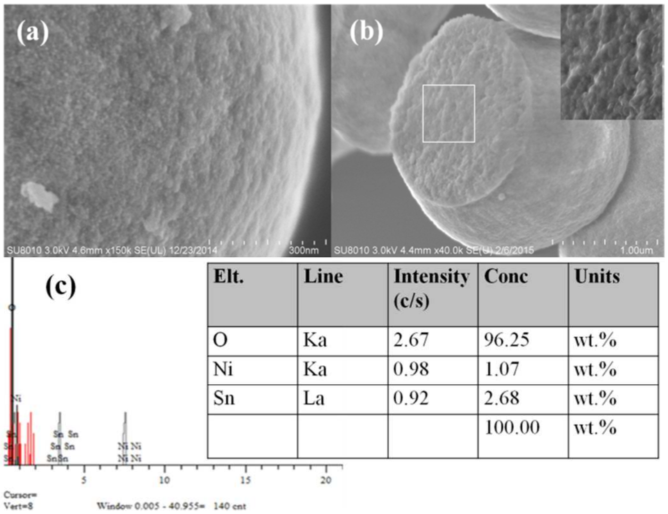

Elt.	Line	Intensity (c/s)	Conc	Units
O	Ka	2.67	96.25	wt.%
Ni	Ka	0.98	1.07	wt.%
Sn	La	0.92	2.68	wt.%
			100.00	wt.%

Fig. 3. (a), (b) SEM images with different magnifications of NDT microspheres (Sn/Ni = 2:1), (c) EDX spectra of NDT microspheres (Sn/Ni = 2:1).

The microstructure of NDT microspheres (Sn/Ni=2:1) has been the compositions of $Sn_{0.67}Ni_{0.33}O_{1.67}$ are investigated by SEM, as showed in Fig. 3. It is clearly that the microspheres' external rough surfaces are composed of tightly packed nanoparticles (Fig. 3a). From the broken sphere in Fig. 3b, we can clearly find that the entire microsphere is agglomerated compactly by small nanocrystals. During the hydrothermal precipitation in the presence of nanocrystals, which are uniformly assembled together into NDT microspheres (Fig. 3b inset). EDS analysis of the sample indicated the presence of Sn, Ni and O elements in the microspheres (Fig. 3c). From the above analysis, it can be concluded that the final composite was Ni doped SnO_2 microspheres.

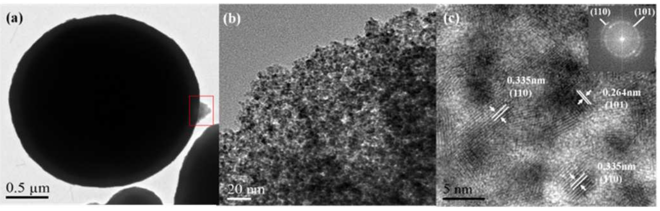

Fig. 4. (a), (b) TEM images of NDT microspheres (Sn/Ni = 2:1), (c) HRTEM image, the inset is the FFT pattern.

To shed light on the morphological feature of the samples, we resort here to transmission electron microscopy (TEM), the results are shown in Fig. 4. The small nanocrystals, as building blocks for the microspheres (Fig. 4a), can be further clearly observed on the edge of microsphere (Fig. 4b). It is the aggregation of these tiny nanocrystals that constituting the NDT microspheres. It is satisfactory and in agreement with the SEM images. The HRTEM image (Fig. 4c) shows that the distances of the lattice fringes over a large area are 0.335 and 0.264 nm, which are in agreement with the lattice spacing of SnO_2 (110) and (101) planes.

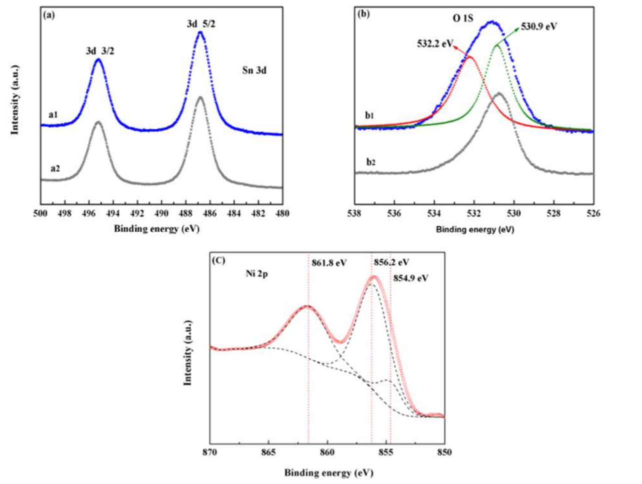

Fig. 5. The corresponding high-resolution XPS spectra of (a) Sn 3d (a1 for NDT microspheres (Sn/Ni = 2:1), a2 for SnO_2), (b) O 1s (b1 for NDT microspheres (Sn/Ni = 2:1), b2 for SnO_2), (c) Ni 2p for NDT microspheres (Sn/Ni = 2:1).

To demonstrate the Ni dopant and its doping levels in the as-prepared NDT microspheres, pure SnO_2 and NDT microspheres (Sn/Ni = 2:1) samples are investigated by XPS. The binding energies (BE) values are measured for the Sn 3d, O 1s, and Ni 2p lines. Fig. 5a shows two peaks located at 486.7 eV and 495.2 eV, which can attribute to Sn $3d_{5/2}$ and $3d_{3/2}$ states respectively.[18,19] It indicates that tin is in the Sn^{4+} statecoordinated by oxygen atoms. Fig. 5b provides the information of binding energies and intensities of the surface element of O 1s of SnO_2 and NDT microspheres (Sn/Ni = 2:1). With the introduction of Ni, the position of the peak shifts to a higher energy compared with pure SnO_2, Thus suggesting the coexistence of different chemical environments. This could be ascribed to some Sn^{4+} replaced by Ni^{2+} of the SnO_2 lattice and the formation of Sn–O–Ni bonds in the NDT samples. The difference in electronegativity (χ) between Sn (χp = 1.96), O (χp = 3.44) and Ni (χp = 1.91) results in a lower electron cloud density of O atoms, thus the binding energy of O 1s (531.1 eV for NDT samples) increases compared to pure SnO_2 (530.9 eV). After peak deconvolution (Fig 5b), the O1s spectra reveal splitting into two bands. The major component at 530.9 eV is typical for the SnO_2 cassiterite network, whereas the second minor band at higher BE (ca. 532.2 eV) is mainly related to the presence of ≡Sn-OH species and/or to the O atoms bonded to the Ni atoms which may arise from some Ni^{2+} replaced Sn^{4+} of the SnO_2 lattice.[20,21] In Fig. 5c, the binding energies may also imply the formation of the NDT microspheres. The Ni 2p XPS peak shows three components, at 854.9, 856.2 and 861.8 eV, which can be referred as the main peak (856.2eV) and the two satellite peaks (854.9 and 861.8 eV).[22-24] The peak at 856.2 eV has been associated with the presence of Ni^{3+} ions,[25] Ni^{2+}-OH species,[26] Ni^{2+} vacancies,[27] or as a result of a non-local screening mechanism, while the satellite peak at 861.8 eV involves a charge transfer ligand-metal.[28,29] Thus, a different local environment of the Ni atoms in the Ni-Sn-O catalyst can be inferred, further indicating the existence of Ni in the sample.

ICP analysis is explored to gain the compositions of the prepared samples. Table 1. provides the metal compositions of the samples measured by ICP-MS. The result shows that the final Sn/Ni molar ratios of all the prepared samples are almost the same with the initial ones.

Sample	During systhesis	From ICP-MS
Sn:Ni=5:1	0.2	0.22
Sn:Ni=4:1	0.25	0.26
Sn:Ni=3:1	0.33	0.32
Sn:Ni=2:1	0.5	0.53
Sn:Ni=1:1	1	1.22

Table 1. The ratios of Ni/Sn from ICP-MS.

The UV-vis diffuse reflectance spectra of the calcined sample NDT microspheres (Sn/Ni = 2:1) is showed in Fig. 6. As can be seen, naked SnO_2 has a good light absorption only in the ultraviolet region, while the NDT microspheres shows better absorption performance in the range of 400–600 nm. It indicates that doped Ni enhanced significantly visible light absorption of SnO_2 catalyst. The direct band gap values of the SnO_2 and NDT microspheres samples are estimated from the $(A h\upsilon)^2$ versus photon energy ($h\upsilon$) plot as showed in the insert of the Fig. 6. The band gap of the composites is estimated to be 3.15 eV, which is lower than that of SnO_2 (3.59 eV). This indicates a band gap narrowing of the SnO_2 due to the introduction of Ni into the matrix of NDT microspheres. It indicates that the samples have potential ability for photocatalytic decomposition of organic contaminants under visible-light irradiation, which is consistent with the apricot color of the sample.

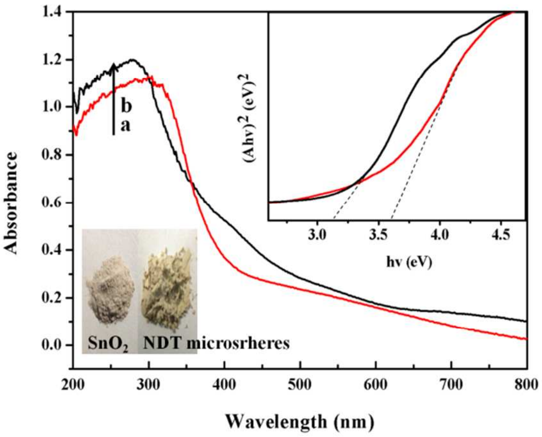

Fig. 6. UV–vis DRS of (a) SnO_2, (b) NDT microspheres (Sn/Ni = 2:1). The inset is band gap evaluation from the plots of $(A h\upsilon)^2$ versus photon energy($h\upsilon$).

FT-IR is used to investigate the functional groups of the as-synthesized samples. The further evidence for the existence of the hydrophilic groups on the surface of samplewithout the calcination come from FT-IR spectra in Fig. 7a, the peak at 3418 and 1628 cm^{-1} are the typical stretching vibration of hydroxyl groups. The intense peaks at 1403 cm^{-1} are assigned to the typical asymmetrical and symmetrical stretching vibrations of C-O because of the COOH groups. The double weaker peaks located at 1033 cm^{-1} is attributed to the C-O-C symmetrical stretching vibrations. The peak at 663 and 494 cm^{-1} are attributed to the Sn-O-H stretching caused by the $Sn(OH)_2$ impurities.[30,31] The most remarkable differences between the three cures are the peaks at 3418 cm^{-1} and 1628 cm^{-1} in Fig. 8a, they disappeared after calcination, showed in Fig. 7b and 7c. The peaks at <1000 cm^{-1} are all attributed to the Sn-O-Sn stretching.[32] Nevertheless, the relative intensity of the peaks decrease after doped nickel, implying that the coordination mode between Ni and SnO_2 alsotransforms versus pure SnO_2.

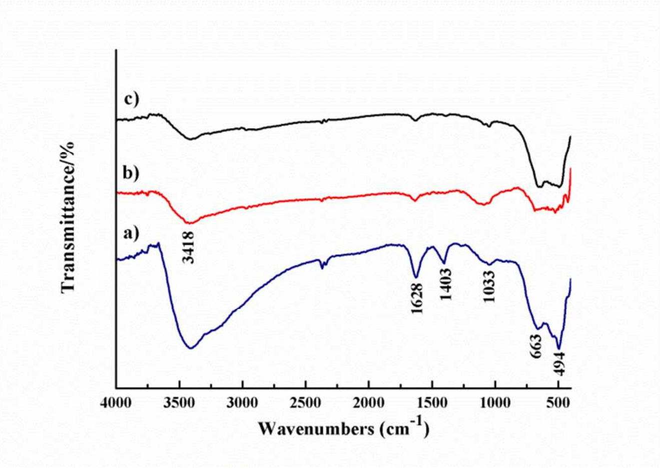

Fig. 7. FTIR spectra of (a) Ni-doped SnO_2 precursor, (b) the corresponding Ni-doped SnO_2 microspheres and (c) SnO_2.

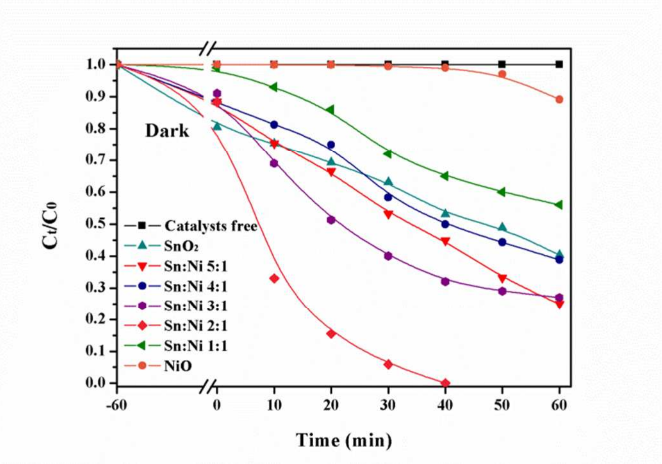

Fig. 8. C_t/C_0 versus time curves of RhB photodegradation under visible light (λ > 420 nm) irradiation over catalyst free, pure SnO_2, pure NiO and Ni-doped SnO_2 microspheres of different molar ratio of Sn/Ni.

Fig. 8 shows the degradation of aqueous RhB (1.0×10^{-5} mol/L) in the presence of 0.05 g of catalystunder visible light (λ > 420 nm) irradiation. C_0 and C_t is the concentrations of RhB aqueous solution at the irradiation times of 0 (that is, after the dark adsorption equilibrium) and t min, respectively. As can be seen from Fig. 8, the photocatalytic activities of the as-prepared NDT microspheres depended on their nickel contents. For example, the decolorization rates of RhB over Sn/Ni = 1:1 is slower than that over SnO_2, but an opposite positive results are obtained by comparison between other doping contents and SnO_2. Besides, no degradation of RhB occurred in the absence ofcatalyst. According to Fig. 8 all the NDT microspheres sample have the highest photocatlyticactivity and shows higher degradation compared to pure NiO. At 40 min the RhB degradation percentage with Sn/Ni = 2:1 was about 100% within the same time period. It is observed that the NDT microspheres (Sn/Ni = 2:1) exhibited betterphotocatalytic performance than pure SnO_2 and other NDT microspheres.

To quantitatively compare the photocatalytic activities of these samples, the reaction rate constants (*k*) are calculated byadopting the pseudofirst-order model as expressed by Eq. (1), which is generally used for photocatalytic degradation processwhen the initial concentration of pollutant is low,[33]

$$\ln(C_0/C_t) = kt \qquad (1)$$

where C_0 and C_t are the concentrations of RhB aqueous solution atirradiation times of 0 and t min, respectively. Table 1 shows the values of *k*. As expected, the *k* values in Table 2 agree with the above analysis results of Fig. 8.

Sample	**Amount of Photocatalysts(g)**	**Concentration of RhB (mol/L)**	***k*** **(min^{-1})**
SnO2	0.05	1.0×10^{-5}	0.015
Sn:Ni=5:1	0.05	1.0×10^{-5}	0.023
Sn:Ni=4:1	0.05	1.0×10^{-5}	0.016
Sn:Ni=3:1	0.05	1.0×10^{-5}	0.022
Sn:Ni=2:1	0.05	1.0×10^{-5}	0.071
Sn:Ni=1:1	0.05	1.0×10^{-5}	0.010

Table 2. Reaction rate constants (k) of samples prepared with different Sn/Ni ratio.

In order to confirm the influence of adsorption, Fig. 9 shows the change of RhB concentration in the presence of catalysts. With an initial RhB concentration of 1.0×10^{-5} mol/L, the adsorption of RhB over Ni-SnO_2 catalysts only reach 15% after stirring for 3 h in dark. Fig. 10 shows the photodegradation of RhB on different catalysts under sunlight irradiation. The catalysts exhibite higher photocatalytic activity than those under visible light, but they show the same tendency, except for pure SnO_2. It is observed that under sunlight, the degradation efficiency of SnO_2 was higher than that of these Ni-doped SnO_2 catalysts, whereas it is exactly the opposite being observed under visible light. Compared with the light sources, the most essential distinctness of them is the existence of UV light in the sunlight. Therefore, we can contribute the relatively higher photocatalytic efficiency of non-doped SnO_2 to the UV light existing in solar light. Thus, the synthesized catalysts should be pointed out to be that, the Ni-doped SnO_2 can be excited by both visible and UV light and exhibited significant degradation efficiency under visible light. It indicates that Ni doping improve the degradation efficiency under visible light irradiation.

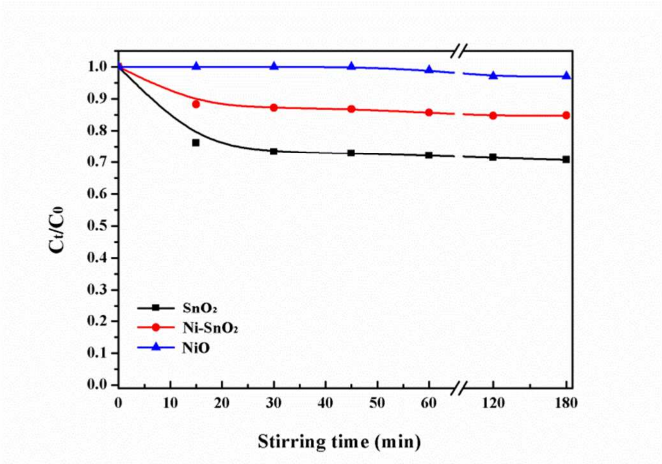

Fig. 9. Concentrations of RhB against stirring time in the dark in the presence of catalysts.

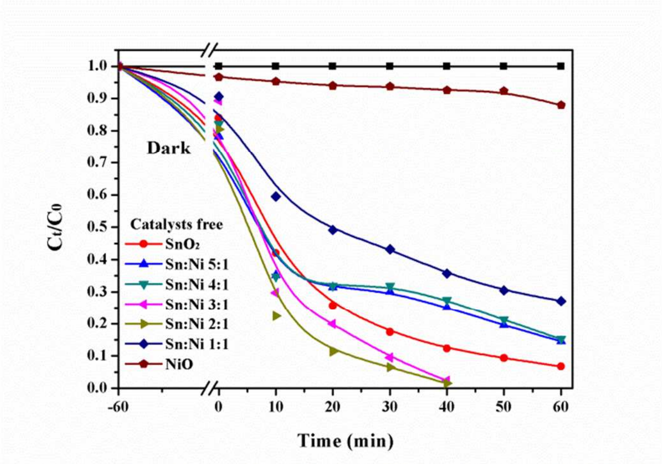

Fig. 10. C_t/C_0 versus time curves of RhB photodegradation under sunlight irradiation over catalyst-free, pure SnO_2, pure NiO and Ni-doped SnO_2 microspheres with different molar ratios of Sn/Ni.

Fig. 11 depicts the temporal evolution of the spectra during thephotodegradation of RhB mediated by the NDT microspheres (Sn/Ni = 2:1) under visible light irradiation (λ > 420 nm). After 5 min irradiation, the maximum absorption band of the solution gradually shiftedand the color of RhB aqueous solution change from pink to light. Meanwhile, the absorption band gradually decreased, which indicates that the ethyl groups of RhB were removedduring irradiation.[34] After reacting for 15–40 min, the adsorption peak of the dye at around 496 nm decreased and the color of dye gradually disappear with the increase of irradiationtime, whereas the hypsochromic shifts of the absorption band are considerably insignificant. It is presumed that the cleavage of thewhole chromophore structure of RhB occurs over the photocatalysts. The result demonstrates that the NDT microspheres could improve the catalytic activity. As shown in Fig. 12, the catalyst can decompose RhB dye efficiently without significant deactivation after fourth times recycling.

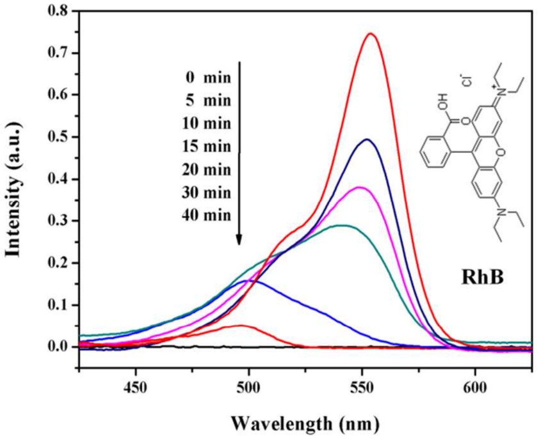

Fig. 11. The temporal evolution of the spectra during the photodegradation of RhB over NDT microspheres (Sn/Ni = 2:1) under visible light (λ > 420 nm) irradiation.

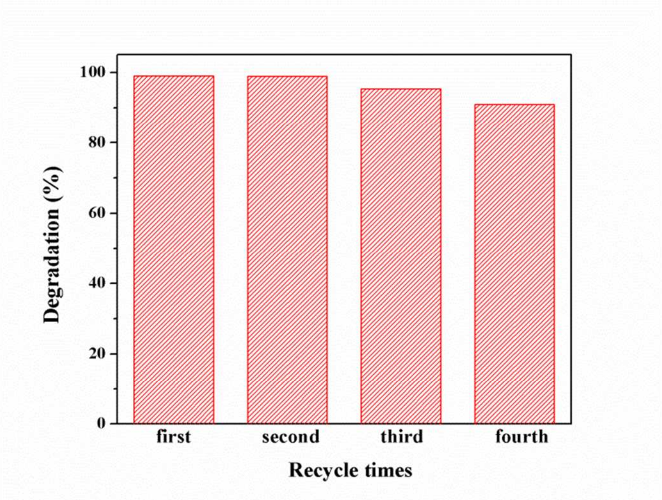

Fig. 12. Degradation percentage of RhB in the presence of NDT microspheres (Sn/Ni = 2:1) under visible light (λ > 420 nm) irradiation.

In order to further insight into the photocatalytic mechanism, we studied the active species involved in the photocatalytic process. Characterised by strong oxidizing, hydroxyl radical (·OH) is deemed to be one of the major active species in the photocatalysis process.[35] By using coumarins as fluorescent probes, the concentration change of ·OH generated on the surface of NDT potocatalysts can be detected according to the following reaction process:

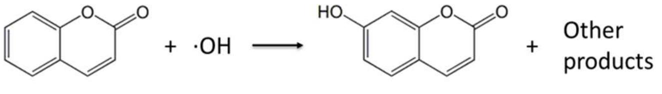

where coumarin is a poorly fluorescent molecule and 7-hydroxycoumarin is a fluorescent one.[36] As shown in Fig. 13, it can be seen that a gradual increase in the PL intensity at about 445 nm with increasing irradiation time. However, no PL intensity increase is observed in the absence of light irradiation or catalyst, which confirms the formation of ·OH during the irradiation process.

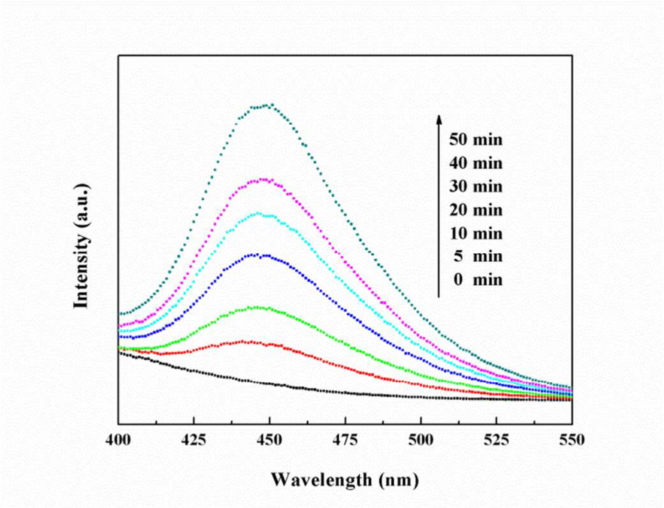

Fig. 13. PL spectra changes observed during visible light illumination of NDT microspheres (Sn/Ni = 2:1) microspheres in a 5×10^{-4} M coumarin solution (excitation at 332 nm).

It is well know that $\cdot O_2^-$ and h^+ can also be generated besides •OH in the photooxidation process.[37] In order to find out which active species dominate the degradation of RhB in the photocatalytic reaction, IPA, BQ and TEOA were introduced as molecular detectors to quench •OH, $\cdot O_2^-$ and h^+, respectively. The produced active species would react with the scavengers preferentially and hinder the photodegradation of RhB. As shown in Fig. 14, the RhB degradation is markedly suppressed in the presence of BQ, suggesting that $\cdot O_2^-$ is primarily responsible for the degradation of RhB. The decrease in photodegradation rate was observed with the addition of IPA and TEOA, which revealed that •OH and h^+ participated in the RhB degradation process. The active species trapping experiments indicate that $\cdot O_2^-$ is the most important reactive specie for RhB degradation.

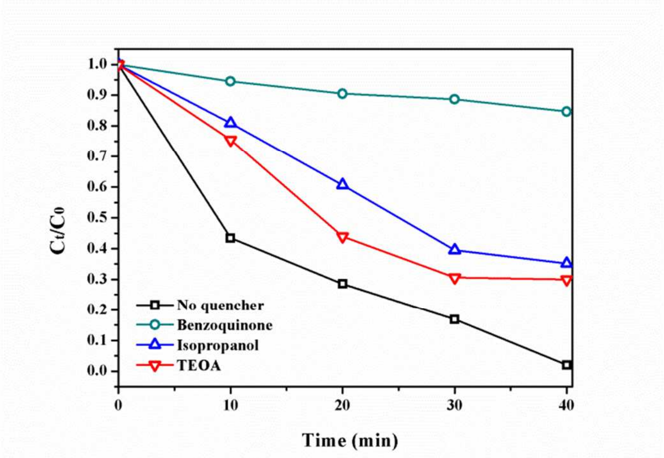

Fig. 14. The photocatalytic activity of NDT microspheres (Sn/Ni = 2:1) microspheres with different quenchers.

Based on the experimental results, we propose a possible two-step growth mechanism for the formation of NDT microspheres. The starting stannum source used in our synthesis is the stannic chloride pentahydrate. First, $Sn(OH)_6^{2-}$ anions are formed by the complexation between Sn^{4+} and OH^- ions, and then the outer surface is oxidized forming SnO_2.[38] In addition, Ni are introduced to the synthesis dissolved in the solution to form $Ni(OH)_4^{2-}$ ions.[39] Under hydrothermal conditions, because smaller seeds with larger curvature possess higher surface energies, and thus increased tendency to aggregate with nanocrystallites, and the process continues until the microspheres are stabilized by lower their surface energy (Fig. 15, Step 1). Finally, the metastable intermediatephase decomposed and recrystallized to form microspheres morphologies.[40] After the sample is subsequently calcined at 350 °C, the release of the hydroxide of the precursor and the oxidation of the organism (Fig. 15, Step 2). We obtain the NDT microspheres structure.

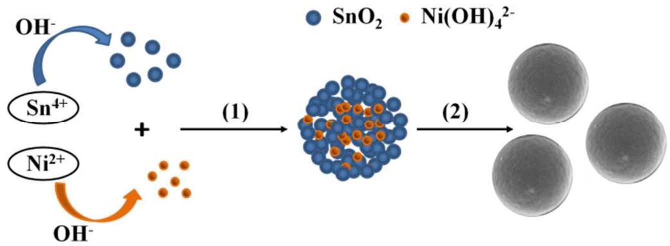

Fig. 15. Illustration of the possible formation mechanism of Ni-doped SnO_2 microspheres.

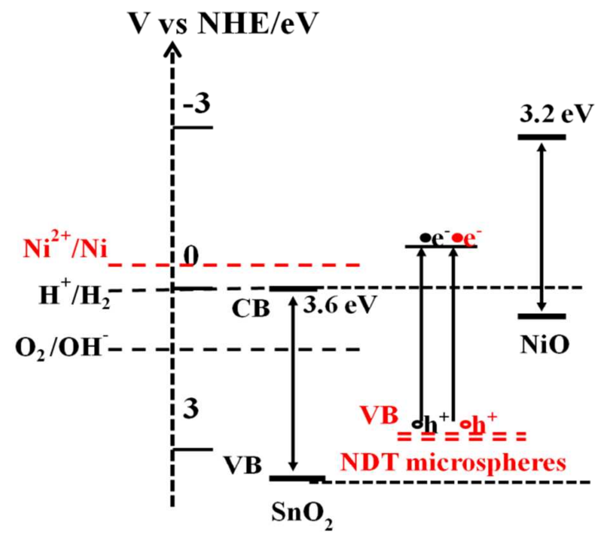

Fig. 16. Conduction and valence band edge potentials of the NDT microspheres (Sn/Ni = 2:1) microspheres.

The calculated CB and VB edge potentials of the NDT microspheres are illustrated in Fig. 16, the following equation is employed:

$$E_{CB} = X\text{-}E^e \text{ -}0.5Eg \qquad (2)$$

$$E_{VB} = E_{CB}+Eg \qquad (3)$$

where X is the electronegativity of the semiconductor which is the geometric mean of the electronegativity of the constituent atoms,[41] E^e is the energy of free electrons on the hydrogen scale, and the value is 4.5 eV, and Eg is the band gap energy of the semiconductor.

It is known that SnO_2 is an n-type direct wide band gap semiconductor (Eg=3.6 eV) while the band gap energy of NiO is 3.2 eV. The conduction band of NiO (–2.7V vs. NHE)[42] is more negative than that of SnO_2 (0.0 V vs. NHE) [43]. The band gap of the NDT microspheres can regulate the contents of Ni and Sn to improve the activity. For the NDT microspheres (Sn/Ni=2) sample, the calculated results are E_{CB}=-0.584 eV, E_{VB} = 2.567eV based on above equation，the band gap detected (3.15 eV) is narrower than that of SnO_2 (3.50 eV), and the CB energy level is more negative than that of SnO_2. Because the potential (-0.26 V vs NHE, pH = 0) of Ni^{2+}/Ni is lower than the CB level of the NDT microspheres, the electrons in the CB can transfer to Ni clusters.[44] These Ni clusters can promote the separation and transfer of electrons, where O_2 is reduced to $\cdot O_2^-$.

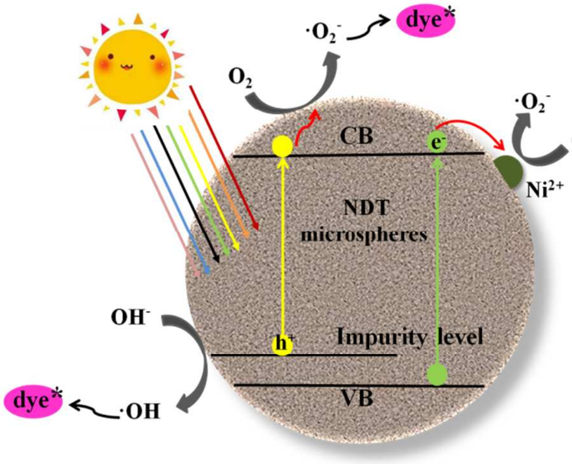

Scheme 1. Diagram of the proposed photocatalytic mechanism of Ni-doped SnO_2 microspheres under visible-lightirradiation.

It is of interest to understand why the NDT microspheres series exhibits the highest photocatalysis activity under identical visible-light irradiation. As we know, the operative basis of photocatalysis is the oxidation-reduction of photogenerated carriers generated by optical excitation on catalysts. The electrons and holes will recombined almost immediately if there is no interference factor. Therefore, the high separation efficiency of photo-generated carriers and wide visible light response range should be the significant reasons that are responsible for this phenomenon.[45] The schematic diagram of the carriers generated and the mechanism of the degradation process over NDT microsphere. The probable mechanism of Ni doping effect is also proposed, which includes two main ways, as shown in Scheme 1. The one is that Ni^{2+} with partially filled d orbital creates an electron donor level in bandgap when they partly entered the SnO_2 lattice, the doped Ni^{2+} can act as atemporary trapping site of photo-induced electrons and greatly suppress the recombination of electron–hole pairs on the surface of the photocatalyst. This is similar to the case for Ni doped TiO_2.[46] The reactive electrons (e^-) from the doped Ni^{2+} reduce O_2 to $\cdot O_2^-$. Meanwhile, the reactive holes (h^+) oxidize RhB to its radical cation either directly or through a primarily formed ·OH produced by the oxidation of ubiquitous water. The other is that the Ni atoms doped in SnO_2 can also promote electron transfer. It is reported that doping can create impurity level close to the valence band edges (dashed line shown in Scheme 1),[47] the doping level of Ni expand the absorption range of light and leading to more photo-generated holes and electrons. The reactive electrons (e^-) from the conduction band reduce O_2 to its radical anion, resulting in the oxidation of RhB at last. NDT possess remarkable broader light absorption region than SnO_2.

Conclusions

Nickel-doped tin dioxide microspheres with different amounts of dopant are hydrothermally synthesized. The catalysts have superior photocatalytic activity in the degradation of RhB under visible light irradiation and shows much higher activity than pure SnO_2 and NiO at room temperature. The sample NDT microspheres with the 33.3% of Ni doping exhibited the highest photoactivity. The high photocatalytic activity can be attributed to the synergistic effect of its demonstrated doping levels as well as the Ni doping. The doping level of Ni of NDT are proposed to be responsible for its high activity. The doped Ni plays a key role in narrowing the band gap and reducing the recombination rate of photon-generated carriers, thus promote the activity and stability of the catalyst. We expect that the method and idea presented in this work will provide a new way for the construction of highly efficient photocatalysts not only for SnO_2, but also for other semiconductor materials.

Acknowledgements

This work was supported by Natural Science Foundation of Hubei Province (2013CFA089).

Notes and references

Key Laboratory of Catalysis and Materials Science of the State Ethnic Affairs Commission & Ministry of Education, Hubei Province, South-Central University for Nationalities, Wuhan 430074, PR China.
*Tel: +86 27 67841302; E-mail: jchu@mail.scuec.edu.cn
† Electronic Supplementary Information (ESI) available. See DOI: 10.1039/b000000x/

1. J. S. Hu, L. L. Ren, Y. G. Guo, H. P. Liang, A. M. Cao, L. J. Wan, and C. L. Bai, *Angew. Chem. Int. Ed.*, 2005, **44**, 1269.
2. K. Lee, D. Kim, P. Roy, I. Paramasivam, B. I. Birajdar, E. Spiecker and P. Schmuki, *J. Am. Chem. Soc.*, 2010, **132**, 1478–1479.
3. G. C. De, A. M. Roy, and S. S. Bhattacharya, *Int. J. Hydrogen energy*, 1996, **21**, 19–23.
4. Y. K. Lai, J. Y. Huang, H. F. Zhang, V. P. Subramaniamb, Y. X. Tangb, D. G. Gongb, L. Sundarb, L. Suna, Z. Chenb and C. J. Lina, *J. Hazard. Mat.*, 2010, **184**, 855–863.
5. S. Ouyang, N. Kikugawa, Z. Zou and J. Ye, *Appl. Cat. A:Gen.,* 2009, **366**,309-314.
6. Y. K. Lai, J. Y. Huang, H. F. Zhang, V. P. Subramaniam, Y. X. Tang, D. G. Gong, L. Sundar, L. Sun, Z. Chen, and C. J. Lin, *J.*

Hazard.Mat., 2010, **184**, 855.

7. S. K. Tripathy, A. Mishra, S. K. Jha, R. Wahab and A. A. Al-Khedhairy, *J. Mater. Sci. Mater. Electron*, 2013, **24** , 2082–2090.
8. Y. M. Lin, R. K. Nagarale, K. C. Klavetter, A. Heller and C. B. Mullins, *J. Mater. Chem.*, 2012, **22**, 11134–11139.
9. J. Duan, S. Yang, H. Liu, J. Gong, H. Huang, X. Zhao, R. Zhang and Y. Du, *J. Am. Chem. Soc.*, 2005, **127**, 6180.
10. M. S. Park, G. X. Wang, Y. M. Kang, D. Wexler, S. X. Dou and H. K. Liu, *Angew. Chem., Int. Ed.*, 2007, **46**, 750−753.
11. J. Y. Huang, L. Zhong, C. M. Wang, J. P. Sullivan, W. Xu, L. Q. Zhang, S. X. Mao, N. S. Hudak, X. H. Liu, A. Subramanian, H. Fan, L. Qi, A. Kushima and J. Li, *Science*, 2010, **330**, 1515−1520.
12. A. T. Kuvarega, R. W. M. Krause, and B. B. Mamba, *J. Phys. Chem. C*, 2011,**115**, 22110.
13. I. Saadeddin, H. S. Hilal, B. Pecquenard, J. Marcus, A. Mansouri, C. Labrugere, M. A. Subramanian and G. Campet, *Solid State Sci.*, 2006, **8**, 7.
14. M. Sorescu, L. Diamandescu and D. Tarabasanu-Mihaila, *Mater. Lett.*, 2005, **59**, 22.
15. L. M. Fang, X. T. Zu, Z. J. Li, S. Zhu, C. M. Liu, W. L. Zhou and L. M.Wang, *J. Alloys Compd* ., 2008, **454**, 261–267.
16. K. Jain, R. P. Pant, S. T. Lakshmikumar, *Sensor. Actuat. B:Chem.*, 2006, **113**, 823–829.
17. X. W. Lou, Y. Wang, C. Yuan, J. Y. Lee and L. A. Archer, *Adv. Mater.*, 2006, **18**, 2325–2329.
18. S. Wu, S. Yuan, L. Shi, Y. Zhao and J. Fang, *J. Colloid. Interf. Sci.*, 2010, **346**, 12–16.
19. H. J. Ahn, H. C. Choi, K. W. Park, S. B. Kim and Y. E. Sung, *J. Phys. Chem. B,* 2004, **108**, 9815–9820.
20. J. F. Moulder, W. F. Stikle, P. E. Sobol and K. D. Bomben, *Handbook of X-Ray Photoelectron Spectroscopy; Perkin Elmer Corp.: Eden Prairie*, *MN,* 1992.
21. R. Kelly , *Surf. Sci.*, 1980, **100**, 85–107.
22. B. Solsona, J. M. L. Nieto, P. Concepción, A. Dejoz, F. Ivars and M. I. Vázquez, *J. Catal.*, 2011, **280**, 28–39.
23. B. Solsona, P. Concepción, S. Hernández, B. Demicol, J. M. L. Nieto, *Catal. Today*, 2012, **180**, 51–58.
24. M. L. Wang, W. W. Liu and C. D. Huang, *Int. J. Hydrogen Energy*, 2009, **34**, 2758–2764.
25. P. Salagre, J. L. G. Fierro, F. Medina and J. E. Sueiras, *J. Mol. Catal. A: Chem.*, 1996, **106**, 125–134.
26. J. C. Vedrine and G. Hollinger, *J. Phys. Chem.*, 1978, **82**, 1515–1520.
27. M. A. Van Veenendaal and G. A. Sawatzky, *Phys. Rev. Lett.*, 1993, **70**, 2459.
28. V. Biju and M. A. Khadar, *J. Nanopart. Res.*, 2002, **4**, 247–253.
29. V. Biju, *Mater. Res. Bull.*, 2007, **42**, 791–796.
30. R. Okawara and M. Wada, *Adv. Organomet. Chem.*, 1967, **5**, 137.
31. Y. Liu, F. Yang and X. Yang, *Colloid. Surface. A.*, 2008, **312**, 219–225.
32. F. Gu, S. F. Wang, C. F. Song, G. J. Zhou, D. Xu and D. R. Yuan, *Chem. Phys. Lett.*, 2003, **372**, 451–454.
33. M. Akarsu, M. ASİLTÜRK and F. Sayilkan, N. KİRAZ4, E. ARPAC and H. SAYILKAN, *Turk. J. Chem.*, 2006, **30**, 333–343.
34. N. U. Silva, T. G. Nunes, M. S. Saraiva, M. S. Saraiva, M. S. Shalamzari and P. D. Vaz, *Appl. Catal. B: Environ.*, 2012, **113**, 180–191.
35. Q. Xiang, J. Yu and P. K. Wong, *J. Colloid Interf. Sci.*, 2011, **357**, 163–167.
36. M. Luo, Y. Liu, J. Hu, J. Li, *ACS appl. Mater. Interf.*, 2012, **4**, 1813–1821.
37. H. W. Huang, X. W. Li, X. Han, N. Tian, Y. H. Zhang and T. R. Zhang, *Phys. Chem. Chem. Phys.*, 2015, **17**, 3673–3679**.**
38. E. R. Leite, T. R. Giraldi, F. M. Pontes, E. Longo, A. Beltrvan and J. Andres, *Appl. Phys. Lett.*, 2003, **83**, 1566–1568.
39. S. Y. Ho, A. S. W. Wong and G. W. Ho, *Crys. Growth Des.*, 2008, **9**, 732–736.
40. J. Hu, K. Zhu, L. Chen, H. Yang and Z. Li, *Adv. Mater.,* 2008, **20**, 267–271.
41. J. Robles and L. J. Bartolotti, *J. Am. Chem. Soc.*, 1984, **106**, 3721–3723.
42. S. Sumikura, S. Mori, S. Shimizu, Shinya, H. Usami and E. Suzuki, *J.Photoch. Photobio. A*, 2008, **199**, 1-7.
43. T. Gao and T. Wang, *Chem Commun*, 2004, **22**, 2558-2559.
44. A. J. Bard, R. Parsons and J. Jordan, Standard Potentials in Aqueous Solution, *Marcel Dekker: New York*, 1985.
45. H. Liu, M. Luo, J. Hu and J. Li, *Sci. Adv. Mater.*, 2013, **5**, 1157–1167.
46. N. S. Begum, H. M. F. Ahmed and K. R. Gunashekar, *B. Mater. Sci.*, 2008, **31**, 747–751.
47. M. A. Rauf, M. A. Meetani, and S. Hisaindee, *Desalination,* 2011, **276**, 13–27.